The Bioscan AN INTERNATIONAL QUARTERLY JOURNAL OF LIFE SCIENCES 20(3): 310-327, 2025 www.thebioscan.com

Synthesis, Characterization, Biological and Electrochemical Applications of Cerium oxide, Iron oxide and its Mixed Metal Oxide Nanoparticles

Gomuraj Santhanaraj[a,b] , Mathavan Alagarsamy[*a], C. Vedhi[*a]

[a]Department of Chemistry, V.O.Chidambaram College, Thoothukudi- 628 008, Tamil Nadu, India.

[b]Research Scholar, Registration No. 17212232031002, Department of Chemistry, V.O.Chidambaram College, Thoothukudi, Affiliated to Manonmaniam Sundaranar University, Abishekapatti, Tirunelveli-627 012, Tamil Nadu, India.

(*Correspondence: Tel: +91 9344315469, Email: abhimathavan@gmail.com, cvedhi23@gmail.com)

DOI: 10.63001/tbs.2025.v20.i03.pp310-327

KEYWORDS
Anti-Bacterial Activity, Cerium Oxide, Iron (III) Oxide, Mixed Metal Oxides And Electrochemical Studies.
Received on:

28-05-2025

Accepted on:

19-06-2025

Published on:

22-07-2025

ABSTRACT

Energy savings and environmental protection depend critically on the detection and monitoring of exhaust and harmful gases. Metal oxide gas sensors are becoming a more popular option because of their high sensitivity and selectivity, which is driving up demand for low-cost, low-power gas sensors. This research work aims to synthesize and characterize metal oxides, specifically cerium oxide, iron(III) oxide, and CFMMO (Ce-Fe), which is a mixed metal oxide consisting of cerium and iron. The synthesis of nanoparticles is accomplished using the co-precipitation method with a microwave reaction system. The resulting nanoparticles are subsequently characterized utilizing various analytical techniques such as FT-IR, UV-VIS (DRS), FE-SEM, EDAX, AFM, and XRD analysis. The XRD pattern confirmed the cubic fluorite structure of CeO_2. In order to investigate the utilization of cerium oxide, iron(III) oxide and cerium iron mixed metal oxides (CFMMO) are used to recognizes of ammonia and hydrogen sulfide with the help of electrochemical method. The binding behavior of metal oxides and ovalbumin were investigated using UV-visible adsorption and fluorescence spectral techniques. The binding constant (K_b), Stern-Volmer constant (K_{sv}), and fluorophore quenching rate constant (k_q) were calculated with the help of spectral data. Using the disc diffusion technique, research has been carried out to investigate the exceptional antibacterial activities of prepared metal oxides and mixed metal oxides against the different bacterial strains.

INTRODUCTION

Metal oxide nanomaterials are thought to be the most important class of materials [1]. Because of their small size, nanoparticles exhibit unique characteristics and behaviors that set them apart from larger counterparts. They are in great demand across a variety of applications due to their distinctiveness [2]. Of the various kinds of nanoparticles, metal oxides and mixed metal oxides have been found to be particularly interesting for a wide range of applications. Metal and oxygen atoms combine to form metal oxide nanoparticles, which are exceptionally small particles [3]. The unique properties of mixed oxide systems, which consist of two or more distinct components, have garnered significant attention due to their inaccessible nature in single components [4]. Metal oxide nanomaterials have superior physical, chemical, and electronic properties than their bulk counterparts, they are becoming more and more valuable in a variety of industries [5]. Metal oxides display the properties of semiconductors, insulators, and metals due to differences in their electronic structures. High-tech and industrial applications heavily depend on metal oxide (MO), whose properties are significantly distorted by factors such as porosity, crystallinity, morphology, doping, and particle size. Numerous metal oxides based on nanomaterials and mixed metal oxides have a wide range of uses, such as environmental remediation, sensors, electronic materials, and catalysis [6].

A novel and straightforward method that provides quick and effective processing of materials with improved reproducibility is microwave-assisted synthesis [7]. In particular, it has become a cost-effective tool for improving dissolution and reducing particle size. The synthesis of inorganic materials has been found to benefit greatly from microwaves' direct molecular reaction and rapid generation of thermal conductivity [8]. Microwave-assisted synthesis is typically carried out in conjunction with a well-established synthesis strategy and operates on the principle of aligning the material's dipoles in an external field via the excitation produced by microwave electromagnetic radiations [9]. The process of alignment or orientation of molecules by the external electrical field may result in the production of internal heat which is responsible for a reduction in processing time and energy required. It is especially due to the heating homogeneity of microwaves [10]. The reaction time can be fairly reduced by adopting microwave-assisted synthesis process. An attempt has been made to synthesize and characterize some of the nanoparticles of metal oxides and mixed metal oxides such as iron oxide, titanium dioxide, cerium oxide and thorium oxide are prepared by chemical precipitation method using microwave reaction system [11].

Because of their exceptional properties and wide range of applications, cerium oxide and iron(III) oxide have garnered significant attention among the various types of metal oxides in

recent years [12]. Owing to their unique and advantageous properties, these metal oxides, cerium oxide and Iron(III) oxide have revolutionized a variety of industries. Furthermore, research into mixed oxides of metals has opened up new avenues for the development of advanced materials with improved performance [13]. Recognizing the characteristics and uses of cerium oxide, iron(III) oxide, and combined metal oxides enables us to capitalize on their potential and continuously push the boundaries of metal oxide technology [14].

Iron oxide nanoparticles (NPs) have recently stimulated the scientific imagination due to their versatile chemical, electrical, optical, and magnetic properties, making it a promising material for a wide range of applications including storage devices, bio-medical applications, catalysts, and magnetic fluids [15]. By maintaining charge neutrality with the oxygen atoms, both the divalent and trivalent cationic states (i.e. ferrous and ferric) assist iron in occurring at different positions in the unit cell. The most common iron oxides are trivalent oxides, which have four crystalline phases, namely α, ß, γ and ε. Among these crystalline phases, hematite (α -Fe_2O_3) is the most stable form of iron oxide, with unusual magnetic properties, non-toxicity, and corrosion resistance [16]. The crystal structure is rhombohedral. Iron oxide-based sensors are widely used in gas detection and air quality monitoring systems due to their high sensitivity and selectivity for various gases. When exposed to a target gas or volatile compound, iron oxide reacts chemically with the analyte, causing changes in its electrical properties [17]. These changes can be used to accurately detect the presence and concentration of specific gases or substances [18]. Iron oxide sensors can be used to detect hazardous gas leaks, ensuring worker safety and preventing potential accidents [19]. Iron oxide nanoparticles can be used to detect specific biomarkers in biological samples, which have enormous potential in early disease diagnosis and personalized medicine [20].

Cerium oxide, also known as ceria, is an oxide of the rare earth metal cerium, denoted by the chemical formula CeO_2. Cerium can exist in either the free metal or oxide form, and can cycle between the cerous-cerium (III) and ceric-cerium (IV) oxidation states [21]. Cerium oxide has a fluorite like cubic structure in which each cerium site is surrounded by 8 oxygen sites in Face centered cubic arrangement and each oxygen site has a tetrahedron cerium site. It exhibits fascinating redox properties and is widely recognized for its catalytic and oxygen storage capabilities. Cerium oxide is commonly utilized as a catalyst in several industrial processes [22]. Its redox property enables it to act as a catalyst in oxidation and reduction reactions, making it an essential component in automotive exhaust catalysts. The ability of cerium oxide to store and release oxygen contributes to efficient and cleaner combustion processes, ultimately reducing harmful emissions [23]. The unique optical properties of cerium oxide also make it a valuable component in optical lenses and glass coatings, providing anti-reflective properties and enhancing light transmission [24]. Cerium and iron mixed metal oxide, often referred to as CFMMO, is a composition of iron(III) oxide (Fe_2O_3) and cerium oxide (CeO_2). This combination results in a powerful material that exhibits remarkable functionality across a variety of applications [25].

The goal of this article was to look into the potential of different metal oxides, specifically cerium oxide, iron(III) oxide and a combination of cerium and iron mixed metal oxides. The use of microwave assisted co-precipitation method to synthesize and characterize these oxides, highlighting their structural characteristics, electrical and optical properties and topography. To accomplish this, X-ray powder diffraction (XRD), field emission scanning electron microscopy (FE-SEM), FT-IR spectroscopy, UV-visible absorption spectroscopy, and atomic force microscopy were used for a thorough examination of the nanoparticles. Recently, there has been a growing interest in the development of gas sensors in a variety of fields such as environmental tracking, manufacturing processes, and medical care. Cerium oxide and iron oxide have received a lot of focus as materials with a lot of potential in gas sensing [26]. Because of their impressive properties, these compounds have received substantial study, making them a good option for the detection of multiple gas types.

Materials and methods

The metal oxides and mixed metal oxides were synthesized using the microwave-assisted co-precipitation technique. All the compounds used in the present research were of the analytical grade. The precursors, namely thorium nitrate ($CeCl_3$ $7H_2O$) and ferric chloride hexahydrate ($FeCl_3.6H_2O$), were obtained from Sigma Aldrich. Sodium hydroxide (NaOH), the precipitant, was acquired from HiMedia. Double-distilled water was used to prepare all the solutions.

Preparation of metal oxides and mixed metal oxides nanomaterials

Synthesis of Cerium oxide (CeO_2)

In a classic synthesis, nanoparticles of cerium oxide (CeO_2) were prepared as follows. First, a solution of 0.1M cerium chloride heptahydrate was prepared using double distilled water. Additionally, a solution of 0.3M sodium hydroxide (NaOH) was also prepared separately. The 0.3M NaOH solution was then slowly added to the 0.1M cerium chloride solution while stirring at a rate of 500 rpm using a magnetic stirrer. Adjustments were made to the revolution of the magnetic teflon as needed to maintain the stirring rate throughout the experiment, especially when the viscous of the mixture increased. The addition continued until the desired pH was reached. Once the addition was complete, the stirring was continued for approximately 2 hours in order to achieve an overall good homogeneity. When cerium chloride heptahydrate reacts with sodium hydroxide, a hydrolysis process occurs and products such as cerium hydroxide are formed. Initially, the aqueous clear solution turns yellowish white, but as the reaction progresses, it converts into a light yellowish colloidal suspension. The solution is then subjected to microwave irradiation using a domestic microwave oven for 15 minutes at 150 W. Afterwards, the irradiated solution is sonicated for 30 minutes at a frequency of 52 kHz in order to obtain better properties of the resulting product. The resulting precipitate is collected through filtration, washed with ethanol followed by distilled water, and dried in a hot air oven at 110°C for 2 hours. The dried powder is subsequently annealed in the muffle furnace at 850°C for 2 hours. During calcination, the cerium hydroxide undergoes degradation and transforming into cerium oxide to acquire a pale yellowish colour.

Synthesis of Iron (III) oxide (α-Fe_2O_3)

In order to synthesize iron(III) oxide nanoparticles, the following steps are carried out. For this preparation, a 0.1M solution of Ferric chloride hexahydrate ($FeCl_3.6H_2O$) and a 0.3M solution of sodium hydroxide (NaOH) were prepared separately using double distilled water. Then, 0.3M NaOH was added dropwise to the 0.1M ferric chloride solution at a stirring rate of 500 rpm using a magnetic stirrer. The addition was maintained until the ideal pH was reached. To ensure good homogeneity, stirring was kept up for around two hours after the addition was finished. The aqueous clear solutions were stirred until a brownish colloidal suspension was formed. After that, the solution was microwave-irradiated for 15 minutes at 150 W using a microwave oven. To enhance the qualities of the synthesized product, the irradiation solution was then sonicated for 30 minutes at a frequency of 52 kHz. After that filtration was used to collect the precipitate, which was then washed with ethanol and distilled water. It was then dried for 2 hours in a hot air oven at 110°C. This dried powder was then annealed for 3 hours in a muffle furnace at 500°C to acquire brown colour pure iron(III) oxide nanoparticles.

Synthesis of Cerium Iron mixed metal oxide (CFMMO)

In this synthesis ferric chloride hexahydrate ($FeCl_3.6H_2O$) and Cerium chloride heptahydrate ($CeCl_3.7H_2O$) were used as precursors. The aqueous solution of 0.1M $FeCl_3$, 0.1M $CeCl_3$ and 0.3M NaOH soluion were prepared using double distilled water separately. The aqueous solution of 0.3M NaOH solution was added drop wise to the solution of 0.1M $FeCl_3$ and stirred well using magnetic stirrer. To this mixture 0.1M $CeCl_3$ solution was added slowly and stirred well for about 2 hours using magnetic stirrer. The solution was then irradiated with microwaves using a microwave oven for 15 minutes at 150 W. Then the irridated solution was sonicated for 30 minutes at 52 kHz frequency and the resulting precipitate was collected by filtration and washed with ethanol followed by distilled water and dried in an hot air oven at 110 °c for 2 hours. This dried powder is then calcined in

the muffle furnace at 850 °C for 3 hours, to get the Cerium iron (CFMMO) mixed metal oxides.

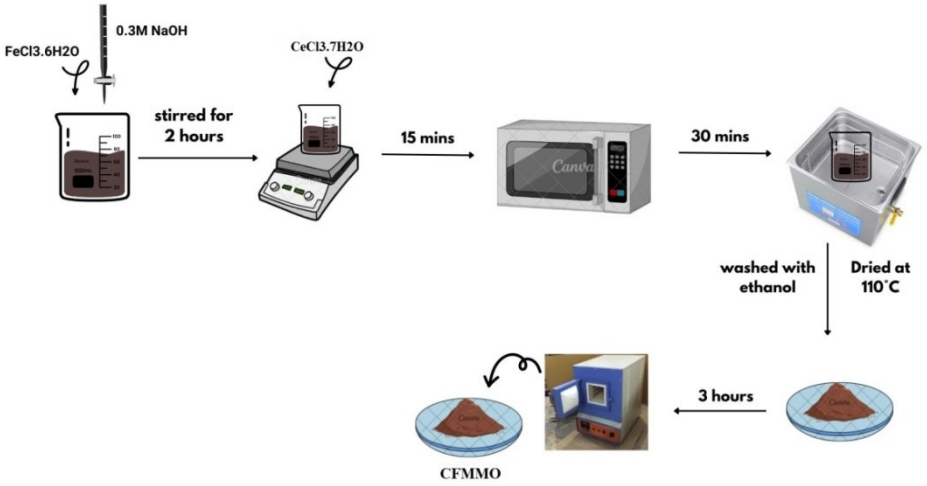

Scheme.1. Schematic diagram of cerium iron mixed metal oxide (CFMMO)

RESULTS AND DISCUSSION

Characterization

The FT-IR spectra in the 4000–400 cm^{-1} range were produced using KBR pellets and a Shimadzu 8400S spectrometer. The XRD data was acquired using a PANalytical X'pert-pro powder X'celerator diffractometer with Cu-kα radiation. UV-visible absorption and fluorescence spectra were analyzed using quartz cells equipped with a JASCO FP-6300 spectrofluorometer and a JASCO variant-630 spectrophotometer. The FE-SEM images were taken using a JEOL JSM-6700F field emission scanning electron microscope. The electrochemical studies were conducted by CH-instrument Inc., a company based in Texas, USA. AFM images were acquired using an Easy Scan 2 controller from Nanosurf, and contact mode measurements were made using a micromachined silicon probe.

In this research, two metal oxide nanoparticles, namely cerium oxide and iron(III) oxide, as well as a cerium iron mixed metal oxide, were synthesized. Then, a variety of analytical methods were used to characterize these nanoparticles. The spectral methods like UV-Visible absorbance (DRS) and FT-IR were used to examine the optical characteristics of the nanoparticles. XRD was used for investigating into the nanoparticles' crystal structure. Energy dispersive X-Ray (EDX) spectrometry and field emission scanning electron microscopy were used to analyze the microstructure, including size, shape, and composition. By using atomic force microscopy, the topography images of the nanoparticles were studied. The data obtained from these analyses are discussed underneath.

Electronic spectra of nanomaterials (DRS)

The technique of measuring the amount of light absorbed by a sample in the UV and visible range is called UV-Visible absorbance analysis, or Diffuse Reflectance Spectroscopy (DRS) [27]. It is a method that clarifies the characteristics of solid materials' absorbance and reflectance throughout the visible and ultraviolet light spectrum [28]. The UV-Visible DRS offers important insights into the chemical makeup, structural characteristics, and optical behavior of a variety of solid samples through the analysis of the spectrum reflectance curves.

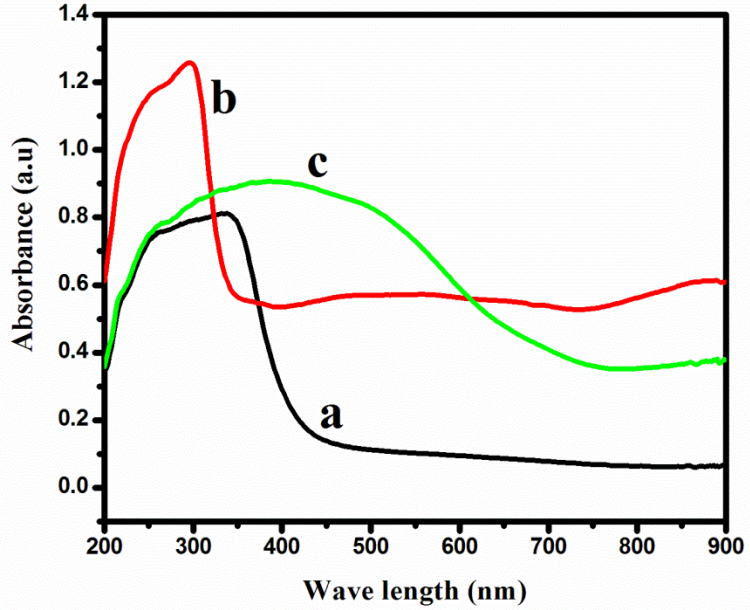

Figure.1. UV-Visible absorbance spectra of (a) CeO_2 (b) Fe_2O_3 and (c) CFMMO

The UV-visible absorption spectroscopy technique was employed to investigate the optical properties of cerium oxide nanoparticles within the wavelength range of 200–900 nm. The obtained results of metal oxides are depicted in Fig. 1(a). A prominent absorbance peak was observed at a wavelength of 336 nm, with an absorbance value of 0.81 (<1), indicating a remarkable UV absorption capability of the synthesized cerium oxide nanoparticles [29]. It is worth noting that the absorbance level is influenced by various factors including band gap, oxygen deficiency, grain size, impurity centers, lattice strain, and surface roughness. The energy band gap of the material was determined utilizing the Kubelka-Munk function, the $(F(R)hv)^2$ was plotted against the hv. The band gap energy of the CeO_2 nanoparticles was quantified using the aforementioned

equation, and the band gap energy of CeO_2 is 2.95 eV. Fig. 1(b) shows that the iron(III) oxide has exhibited a significant absorbance peak at 305 nm, with absorbance value is 1.28 which indicating the remarkable UV absorption capacity of the synthesized iron(III) oxide nanoparticles. The band gap energy of iron(III) oxide was measured and found to be 2.25 eV [30]. The analysis of the spectra showed that the mixed metal oxide had a noticeable broad peak at 395 nm, which indicates a strong absorbance in the visible region (A=0.90). This indicates that the good absorption capacity in the visible range. The band gap energy of the CFMMO nanoparticles was determined to be 2.00 eV [Fig.1(c)].

Fourier Transform – Infra Red Spectral Analysis

FT-IR spectroscopy serves as a valuable tool for identifying functional groups and examining the vibrational movement of atoms and molecules [31]. This technique allows molecules to selectively absorb specific frequencies of infrared (IR) light, which are determined by their unique characteristics. The FT-IR spectra of CeO_2, Fe_2O_3 and mixed oxides of Ce and Fe are given in Figure.2.

The FT-IR spectra exhibited numerous significant absorption peaks within the 4000 cm^{-1} to 500 cm^{-1} range. The absorption peak spanning from 3437.11 cm^{-1} is attributed to the -OH stretching vibrations of H_2O [32]. The peaks at 1448 cm^{-1} and 1630 cm^{-1} absorption bands corresponding to physically adsorbed water molecules [33]. The FT-IR bands is appeared at 879.72 cm^{-1} and 461.43 cm^{-1}, which indicating the presence of CeO_2, which is characteristic of the Ce-O stretching vibrations [Fig. 2(a)]. The large broad band across 3435.28 cm^{-1} is ascribed to the O-H stretching vibration, indicating the presence of H_2O. The absorption picks around 1627.96 cm^{-1} are due to the bending vibration of hydroxyl groups [34]. The strong band below 700 cm^{-1} is assigned Fe-O stretching mode. The band corresponding to Fe-O stretching mode of iron oxide is seen at 566.15 cm^{-1} and 475.25 cm^{-1}. The FT-IR spectra of Cerium Iron mixed metal oxides are given in Fig.2 which displayed an absorption bands at 3443.85 cm^{-1}, indicating the O-H stretching vibration. In addition, the bending vibration of O-H was indicated by the absorption bands at 1592.74 cm^{-1}. The formation of the M-O stretching band of CFMMO is indicated by the strong peaks at 852.93 cm^{-1} and 466.81 cm^{-1} [35]. In the end, this indicates that cerium (Ce-O) and iron (Fe-O) may combine to form a mixed metal oxide.

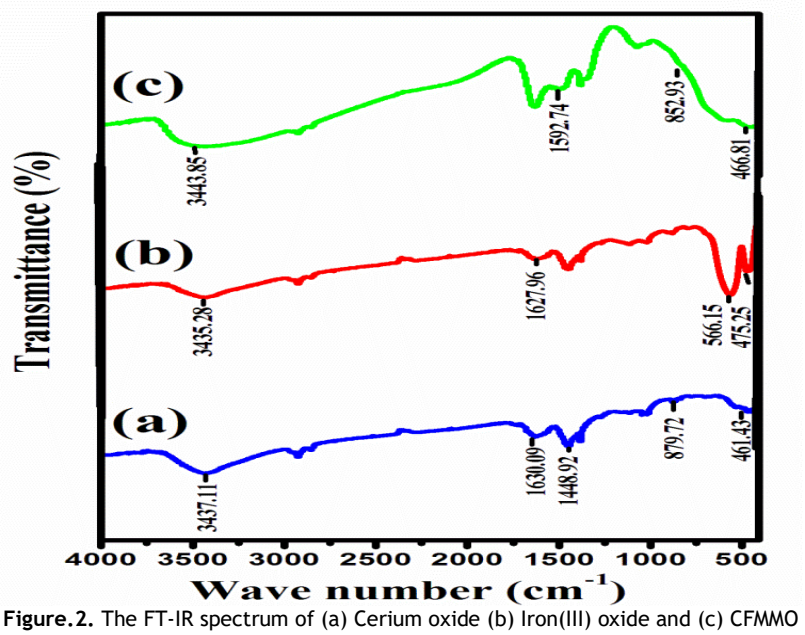

Figure.2. The FT-IR spectrum of (a) Cerium oxide (b) Iron(III) oxide and (c) CFMMO

Table.1. FT-IR spectral data for (1) Cerium oxide, (2) Iron(III) oxide and (3) CFMMO.

S.No	Name of the samples	Assigned functional groups		
		O-H Stretching vibration (cm^{-1})	O-H bending vibration (cm^{-1})	M-O stretching vibration (cm^{-1})
1	Cerium oxide	3437.11	1448.92, 1630.09	461.43 879.72
2	Iron(III) oxide	3435.28	1627.96	475.25 566.15
3	CFMMO	3443.85	1592.74	852.93 466.81

X-ray Diffraction Analysis

X-ray diffraction analysis, also known as XRD analysis, is a non-destructive technique used to determine the arrangement of atoms or molecules within a crystalline material [36]. The crystallinity of the synthesized metal oxide and mixed metal oxide samples were assessed using X-ray diffraction analysis [37]. The X-ray diffraction pattern of the CeO_2 particles was displayed in the Figure 3(a). The structural identification of the cerium oxide nanoparticles was conducted by analyzing the X-ray diffraction within the 2θ range of 20° to 80°. The diffraction pattern was exhibited distinct peaks corresponding to (111), (200), (220), (311), (222), (400), (331), and (422) planes, which indicated that the CeO_2 has exhibited the face-centered cubic fluorite structure. These peaks matched perfectly with the pure cubic fluorite structure of CeO_2, with a lattice constant of a=5.411 Å, aligning with the JCPDS file No. 75-0076 [38]. The particle size of the cerium oxide nanoparticles was estimated using Scherrer's equation: $D_{hkl} = 0.899\ \lambda\ /\ \beta \cos\theta$, where λ represents the X-ray wavelength, θ is the Bragg diffraction angle, and β corresponds to the full width half maximum (FWHM) of the XRD peak observed at the diffraction angle θ. This calculation is yielded the average crystalline size of CeO_2 and it was approximately 17.06 nm.

The XRD pattern of calcined iron(III) oxide nanoparticles is presented in [Figure 3(b)]. The XRD results for the iron oxide nanoparticles exhibits strong peaks around 2θ = 24.13° (012),

33.24° (104), 35.70° (110), 40.54° (113), 49.55° (024), 54.17° (116), 57.44° (018), 62.58° (214) and 64.51° (300). All the diffraction peaks in the XRD pattern are well indexed to the planes of a face centered rhombohedral lattice of α-Fe_2O_3 nanoparticles (JCPDS file No. 33-0664) [39]. The complete transformation of iron hydroxides into hematite (iron oxide) nanoparticles is indicated by the absence of diffraction peaks corresponding to $Fe(OH)_2$ and $Fe(OH)_3$. The absence of any other peaks related to the other phases of iron oxides suggests that the prepared α-Fe_2O_3 nanoparticles were highly pure. The narrow sharp peaks indicates that the hematite products are highly crystalline, implying that the high purity of synthesized hematite particles is obtained by using this synthesis method [40]. The mean crystallite size for the as-synthesized α -Fe_2O_3 nanoparticles was approximately 28.02 nm. Results of XRD analysis clearly indicates that the formation of pure crystalline form α -Fe_2O_3 nanoparticles. To determine the structural identity of the CFMMO nanoparticles, the diffraction peaks at 28.55°, 33.24°, 35.70°, 47.20°, and 56.37° of mixed oxides was observed at certain crystallographic planes of (111), (104), (110), (220) and (311) in CFMMO [fig.3 (c)]. Thus, applying Scherrer's equation, the average crystalline size was determined to be roughly 29.65 nm.

Energy-Dispersive X-Ray Analysis (EDAX)

The determination of the elemental composition of metal oxides and mixed metal oxides was conducted using Energy Dispersive X-ray Spectroscopy (EDS) [41]. This analytical technique involves the recording of characteristic X-rays by an energy dispersive spectrometer, enabling the identification of elements present as well as assessing their respective concentrations [42]. The EDS, is employed in conjunction with Scanning Electron Microscopy (SEM), enabled the examination of the chemical composition of the material. The analysis of CeO_2 using Energy Dispersive Spectroscopy (EDS) is presented in Figure 4 (a). The obtained EDS spectrum clearly exhibits peaks corresponding to cerium and oxygen, indicating their existence within the sample. The weight concentration of cerium and oxygen, accounting for a total of 96.86%, further ensures the high purity of the cerium oxide nanoparticles. The energy dispersive spectrum (EDS) of α-Fe_2O_3 prepared by microwave-assisted co-precipitation method is shown in [Fig.4 (b)] which confirms the existence of Fe and O with weight percent and atomic percent. All the measurements were carried out at room temperature. The peak at 6.4 keV shows the presence of iron and the peak at 0.5 keV for oxygen clearly shows the elemental composition and purity of α-Fe_2O_3 nanoparticles and the results of EDS analysis clearly which indicates that the formation of pure crystalline α-Fe_2O_3 nanoparticles [43]. Iron (70.79%) and oxygen (29.21%) by weight percentage were the elements that made up the iron oxide elemental composition. The weight concentration of iron and oxygen, accounting for a total of 100.00%, further ensures the high purity of the iron oxide nanoparticles without any contamination.

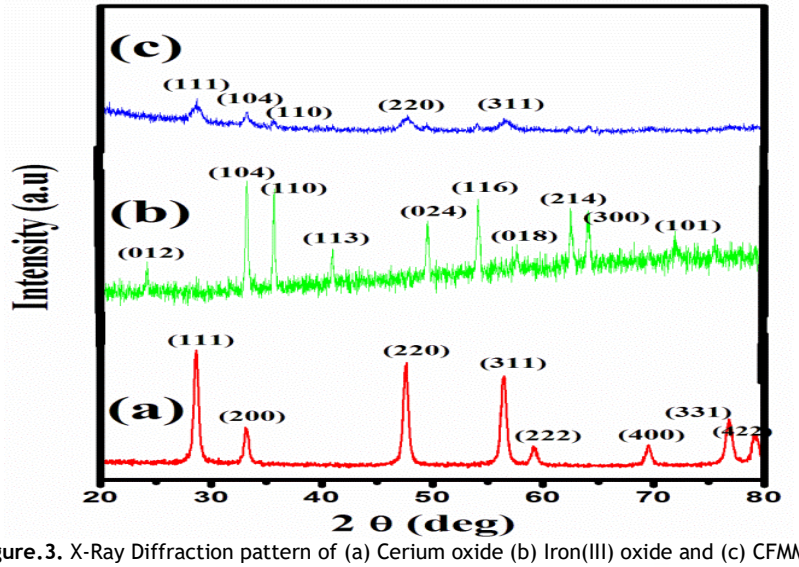

Figure.3. X-Ray Diffraction pattern of (a) Cerium oxide (b) Iron(III) oxide and (c) CFMMO

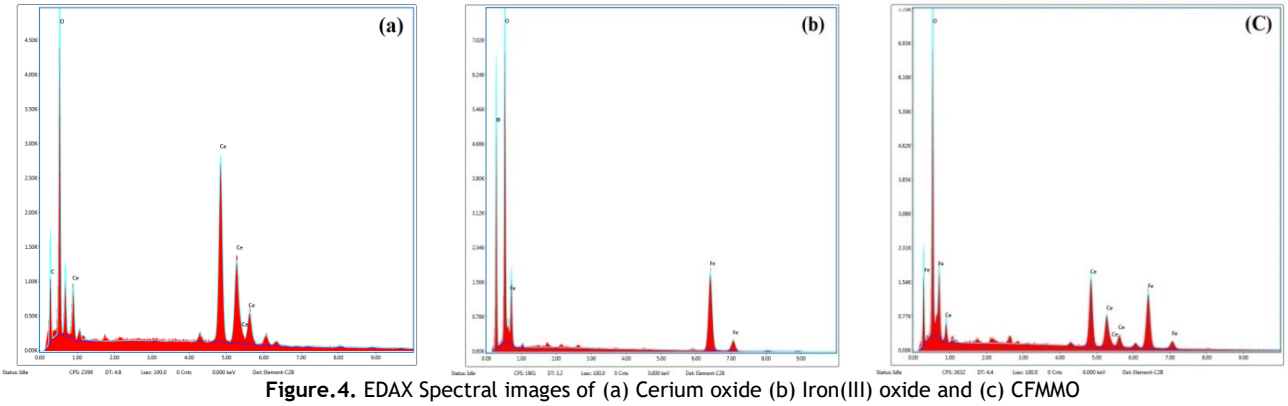

Figure.4. EDAX Spectral images of (a) Cerium oxide (b) Iron(III) oxide and (c) CFMMO

In both weight percent and atomic percent, cerium, iron, and oxygen have been identified in CFMMO according to energy dispersive spectroscopy (EDS) analysis. As displayed in [Fig. 4 (c)], the EDS analysis reveals distinct peaks corresponding to the elements cerium, iron, and oxygen. The presence of cerium at 5.0 keV, iron at 6.4 keV, and oxygen at 0.5 keV is clearly shown in the obtained EDS spectrum, confirming the near-purity of the cerium iron mixed metal oxide nanoparticles . This finding is further supported by the weight concentrations of cerium, iron, and oxygen, which sum to 100.00% and comprise 44.95% cerium, 35.35% iron, and 19.69% oxygen overall.

Table.2. Elemental composition of (a) Cerium oxide (b) Iron(III) oxide and (c) CFMMO

a) Cerium oxide			b) Iron(III) oxide			c) CFMMO		
Element	**Weight %**	**Atomic %**	**Element**	**Weight %**	**Atomic %**	**Element**	**Weight %**	**Atomic %**
C K	3.14	20.48	***	***	***	**O K**	19.69	45.32
O K	16.45	49.40	**O K**	29.21	35.98	**Ce L**	44.95	11.81
Ce L	80.41	30.12	**Fe K**	70.79	64.02	**Fe K**	35.35	42.87
Total	100	100	**Total**	100	100	**Total**	100	100

Field Emission Scanning Electron Microscope analysis:

The investigation into the morphology and structure of the samples was carried out utilizing Field Emission Scanning Electron Microscopy (FE-SEM) [44]. The FE-SEM images of CeO_2, Fe_2O_3 and mixed oxides are exhibited in the Figure 5.

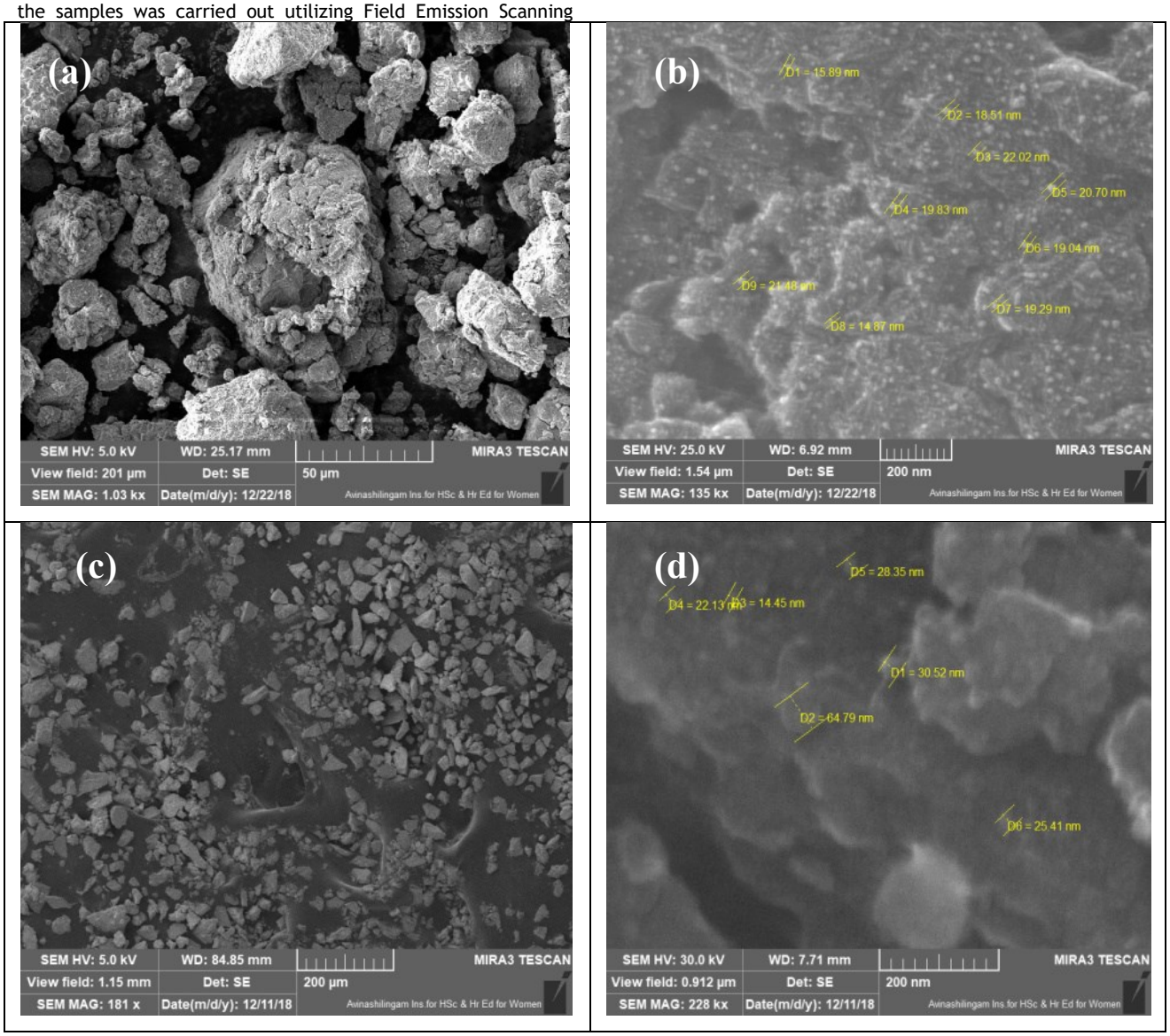

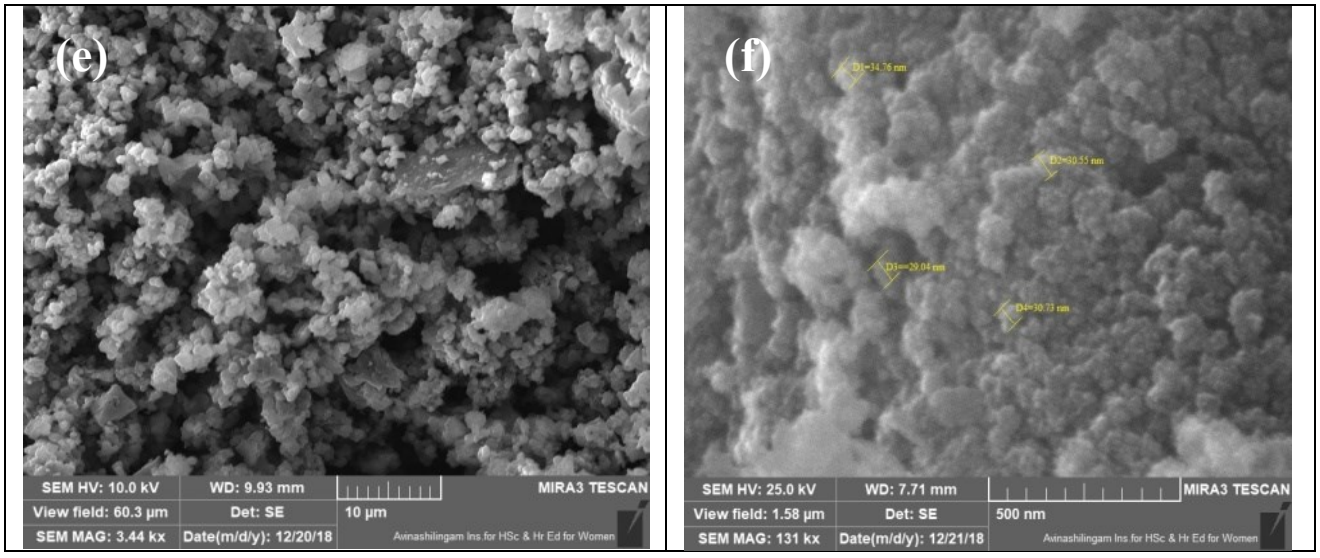

Figure.5. Shows the FESEM images of (a-b) Cerium oxide, (c-d) Iron(III) oxide, (e-f) CFMMO

The surface analysis of prepared CeO_2 was involved in the measurement of SEM micrographs and subsequent topographical analysis [45]. The FE-SEM images reveals that the prepared nanomaterials were uniform in size, shape and not agglomerated. The results revealed that the synthesized CeO_2 nanoparticles exhibited a uniformly sponge like shape with a smooth and homogeneous structure. The average particle size estimated from FE-SEM images is about 20 nm (fig.5a). The FE-SEM images of the α-Fe_2O_3 nanoparticles synthesized using the microwave-assisted co-precipitation method are displayed in Fig.5 (a-b). The prepared sample is apparent in this figure magnified by 200 µm, forming a structure that appears to be a small flake shaped particles and are well crystallize in nature [46]. The average particle size estimated from FE-SEM images of α-Fe_2O_3 is about 30 nm [Fig.5 (b)]. At 10 µm magnification, the prepared CFMMO displayed a cloud-like structure with an average particle size of 28 nm [Fig.5 (c)]. The microscope allows for the study of clear, high to low magnification images down to the nanometer range [47].

Atomic Force Microscope spectral analysis

AFM is a vital tool in nanotechnology for the design and characterization of nanoscale structures [48]. The Atomic Force Microscope employs a cantilever with a sharp tip to scan the surface of a sample at the atomic level. By measuring the forces between the tip and the sample, AFM generates high-resolution three-dimensional images of nanoscale structures. It is a vital instrument for exploring phenomena at the nanoscale since it can resolve characteristics all the way down to the atomic size [49]. Using an atomic force microscope, the prepared nanomaterials' morphology was examined. Every scan was carried out in ambient conditions, which are known to produce topography results that are satisfactory. With a resolution of 256x256 pixels and a scan rate ranging from 0.5 to 1 Hz, the images were captured in topography mode. Using the microscope's section analysis software, the heights of adsorbed NPs and agglomerates were measured [50]. The AFM images of CeO_2, Fe_2O_3 and mixed oxides of Ce and Fe are given in the figure.6. The image reveals that the prepared nanomaterials has well separated nano dot like structure. To characterize the surface topography, the roughness parameters are very essential. Table 3 lists the most common parameters of area roughness. The average roughness (S_a) and the root mean square roughness (S_q) are evaluated over the complete 3D surface respectively. Particularly, root mean square roughness (S_q) is used to study the temporal changes in the creation of a new surface as well as spatial differences when studying the surface feature using different scales. As the image illustrates, the AFM images of α-Fe_2O_3 reveals a well-separated group of conical nano columnar structure. The morphology of the synthesized mixed metal oxide was investigated with an atomic force microscope. A cloud like structure can be seen in the CFMMO AFM images. These structures are further examined by the 3-D view of AFM which is shown in Fig.7.

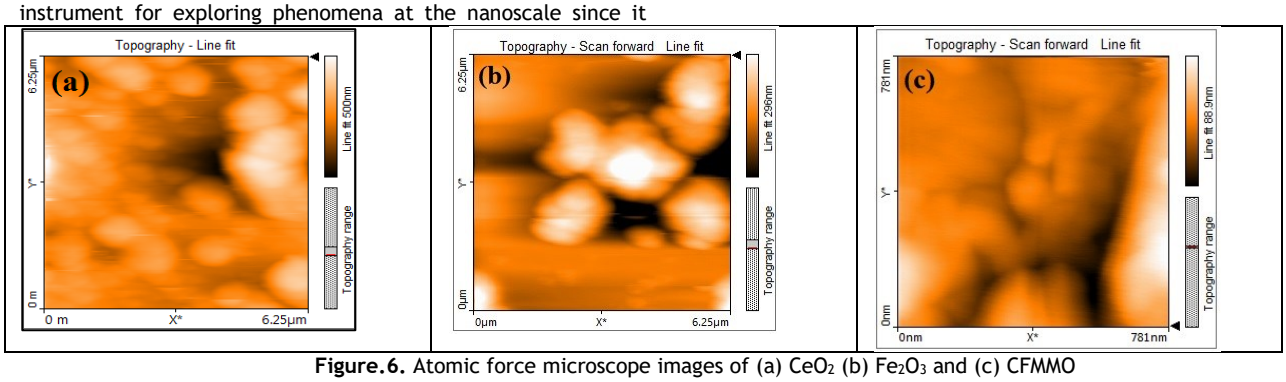

Figure.6. Atomic force microscope images of (a) CeO_2 (b) Fe_2O_3 and (c) CFMMO

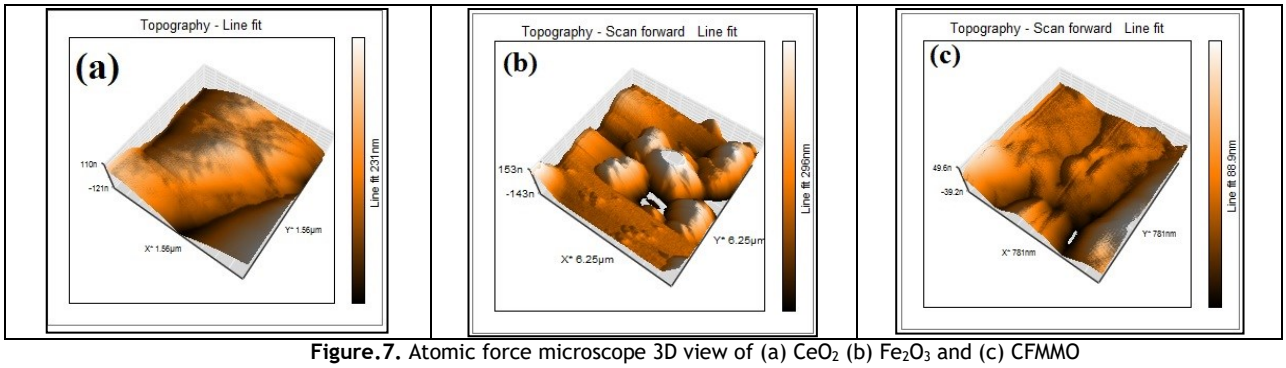

Figure.7. Atomic force microscope 3D view of (a) CeO_2 (b) Fe_2O_3 and (c) CFMMO

Table.3. Area roughness of Cerium oxide, Iron(III) oxide and CFMMO from AFM spectroscopy

Area Roughness			
Area Parameter	**CeO_2**	**Fe_2O_3**	**CFMMO**
Area	39.37 pm^2	39.37 pm^2	615.1 fm^2
S_a	54.07 nm	45.44 nm	10.75 nm
S_q	71.39 nm	64.69 nm	15.04 nm
S_y	498.70 nm	499 nm	94.59 nm
S_p	249.74 nm	226.25 nm	52.64 nm
S_v	-248.93 nm	-272.74 nm	-41.94 nm
S_m	-35.91 fm	-18.62 fm	-20.47 fm

Sensing analysis of Cerium oxide, Iron(III) oxide and Cerium iron mixed metal oxides (CFMMO)

Metal oxide gas sensing works by adsorbing gas molecules onto the surface of a metal oxide sensor. Typical industrial operations and emissions include the production of ammonia and hydrogen sulfide gas. Even though these gases might not be apparent to the human eye, prolonged exposure to large quantities of them might have detrimental effects on health [51]. When this sensor interacts with a specific gas, a chemical reaction takes place, causing a change in electrical conductivity [52]. This change in conductivity is carefully measured and analyzed to accurately determine the presence of the particular gas.

Electrochemical Applications

The method of measuring the current response to an applied voltage in the presence of gas is known as cyclic voltammetry gas sensing. Analyzing the redox processes at the electrode-gas interface can be done by applying a potential sweep to an electrode and measuring the current that results. The purpose of this study was to assess the sensing ability of metal oxides to detect NH_3 and H_2S gas. In this work, voltammetric analyses were carried out by using buffer solution pH-7.00 with the help of glassy carbon electrodes. A CH-instrument Inc. was used for the CV measurements with a cell consisting three electrodes like a glassy carbon electrode (working electrode), platinum wire (counter electrode), and a saturated calomel electrode (reference electrode) [53]. The overall potential range between -1.6 V and +1.2 V was carried out at a scan rate of 20 mV/s.

Recognition of ammonia (NH_3)

The synthesized nanomaterials were subjected to cyclic voltammogramms with a scanning range of -1.6 V to 1.2 V. The Cyclic Voltammogram of ammonia on modified GCE containing metal oxides like cerium oxide, iron(III) oxide and CFMMO were designated as (a), (b) and (c) respectively and shown in Figure 8. During the cyclic voltammograms the modified GCE containing metal oxides like cerium oxide, iron(III) oxide and CFMMO showed a reduction peak due to their designated oxygen storage capacity, which was designated as (I), and shown in cyclic voltammograms of (a), (b) and (c) and the respected peak current values are shown in Table 4. The addition of 1 mM of ammonia solution to the system resulted in a cathodic peak current shift and the transformation of the broad peak into a distinct and narrow peak, indicating an increasing peak current value due to the adsorption of ammonia on the surface of the electrode [54, 55]. This change clearly demonstrated the sensing capability of CeO_2, Fe_2O_3 and CFMMO towards ammonia, referred to as (II), and shown in cyclic voltammograms of (a), (b) and (c) and the corresponding peak current values are shown in Table 4. In comparison to the cathodic peak current values of cerium oxide (E = 0.58 V and i = 5.96 e^{-6}A) and iron oxide (E = 0.75 V and i = 6.50 e^{-6}A), CFMMO exhibits higher peak current values of E = 0.40 V and i = 8.96 e^{-6}A. This indicates to CFMMO's better ammonia sensing ability over that of cerium oxide and iron oxide. For the cyclic voltammograms, the overall potential scan rate was 20 mV/s.

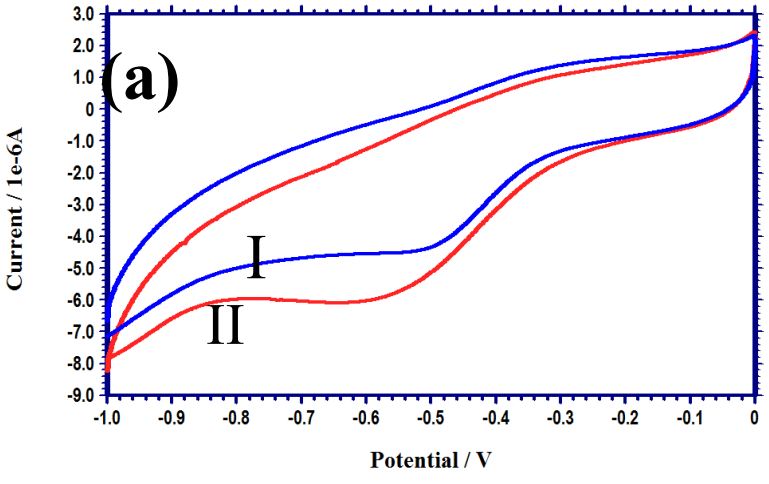

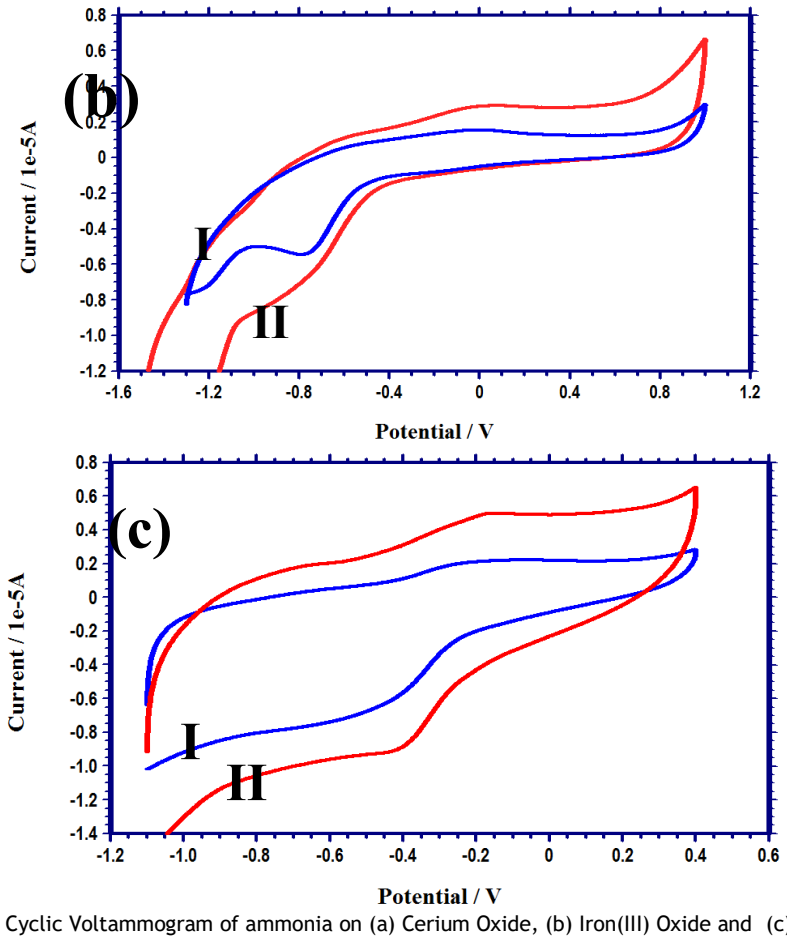

Figure.8. Cyclic Voltammogram of ammonia on (a) Cerium Oxide, (b) Iron(III) Oxide and (c) CFMMO

Table.4. Cyclic voltammogram behavior of ammonia [Ph=7.00, scan rate=20 mV/s]

S.No	Types of Electrode	Cathodic Peak current of Modified GCE (I)		Cathodic Peak current of Modified GCE Ammonia (II)	
		$-E_{pc}$ (mV)	$-i_{pc}$ (μA)	$-E_{pc}$ (mV)	$-i_{pc}$ (μA)
a	Cerium oxide Modified GCE	0.51	4.42	0.58	5.96
b	Iron(III) oxide Modified GCE	0.75	5.16	0.76	6.50
c	CFMMO Modified GCE	0.45	6.37	0.40	8.96

Recognition of Hydrogen sulfide (H_2S)

Cyclic voltammograms of prepared nanomaterials was scanned from -1.6 V to 0.8 V. The potential scan rate for the cyclic voltammograms was 20 mV/s. The Cyclic Voltammogram of Hydrogen sulfide on modified GCE containing metal oxides like cerium oxide, iron(III) oxide and CFMMO were designated as (a), (b) and (c) respectively and shown in Figure 9. A lower response in cathodic peak current was observed when the GCE was modified with metal oxides like cerium oxide, iron(III) oxide and CFMMO, which was denoted as (I), and shown in cyclic voltammograms of (a), (b) and (c) respectively and the depicted peak current values are shown in Table 5. After the introduction of 1 mM of H_2S solution to the cell, the observed peak current exhibited a noticeable shift and showed an increase in peak current value due to the adsorption of H_2S on the surface of the electrode [56, 57]. This increase in peak current signifies the successful sensing ability of CeO_2, Fe_2O_3 and CFMMO towards H_2S, which was denoted as (II) and shown in cyclic voltammograms of (a), (b) and (c) respectively and the displayed peak current values are shown in Table 5. Additionally, the mixed metal oxide of CFMMO showed a peak current of E=0.75 V and i=9.05e^{-5}A, indicating a higher H_2S adsorption in comparison to cerium oxide and iron oxide. It is also evident that CFMMO's better H_2S sensing abilities are supported by its higher peak current values (E = 0.75 V and i = 9.05 e^{-5}A) compared to cerium oxide (E = 1.00 V and i = 1.50 e^{-5}A) and iron oxide (E = 0.79 V and i = 9.00 e^{-5}A).

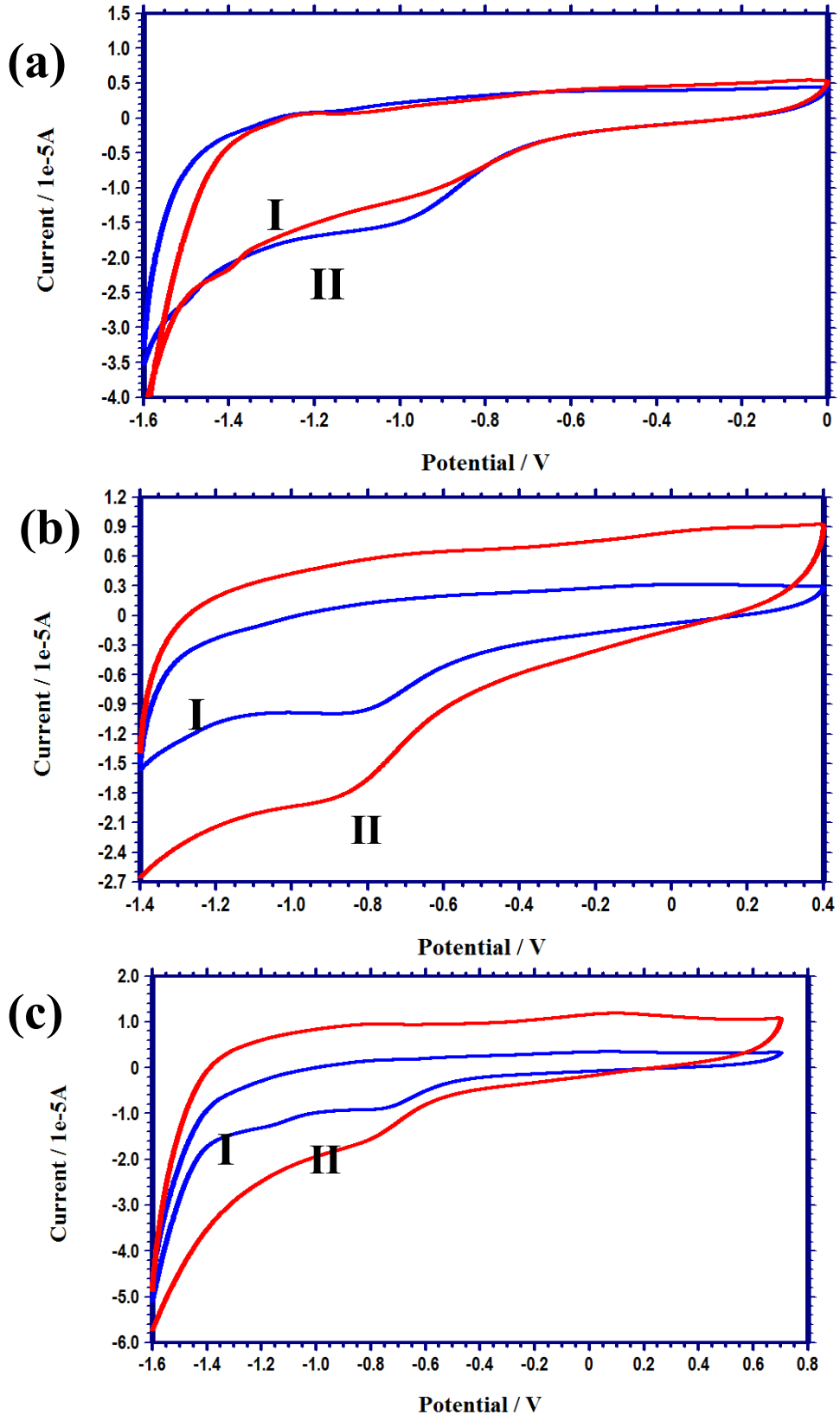

Figure.9. Cyclic Voltammogram of H_2S on (a) Cerium oxide, (b) Iron(III) oxide and (c) CFMMO.

Table.5. Cyclic voltammogram behavior of Hydrogen sulfide [Ph=7.00, scan rate=20 mV/s]

S.No	Types of Electrode	Cathodic Peak current of Modified GCE (I)	Cathodic Peak current of Modified GCE + Addition of Hydrogen sulfide (II)

		$-E_{pc}$ (mV)	$-i_{pc}$ (μA)	$-E_{pc}$ (mV)	$-i_{pc}$ (μA)
a	Cerium oxide Modified GCE	1.03	1.20	1.04	1.50
b	Iron(III) oxide Modified GCE	0.86	1.81	0.79	9.00
c	CFMMO Modified GCE	0.81	1.62	0.75	9.05

Biophysical interaction of ovalbumin

One of the main proteins in egg whites, ovalbumin has shown to be a useful model system for researching interactions between proteins and surfaces. An area of focus for research is determining Ovalbumin's affinity for metal oxide surfaces for binding. It is impossible to overestimate the importance of understanding molecular binding interactions in protein research [58]. Examining the Ovalbumin binding interactions by using the UV-visible absorption spectral titrations is a fascinating area of study in this field [59].

UV-Visible absorption spectral responses of Ovalbumin

The UV-Visible absorption spectral responses of Ovalbumin have been extensively studied to understand its behavior and applications. In the UV-Visible absorption spectral titrations, a metal oxide was gradually added to a protein solution while the absorbance spectral changes was being studied. This method provides useful data regarding the interaction's stoichiometry, thermodynamics, and binding affinity. The binding constant (K*a*) value is derived from the changes in the absorption spectrum of Ovalbumin at 209 nm, in which the absorbance decreases was due to the binding interaction between proteins and nanoparticles. The ovalbumin concentration (20 μM) was maintained constant while the nanoparticle concentration ranged from 0 to 30 μM during the spectral titrations. The UV-visible absorption spectra of ovalbumin with the addition of nanoparticles are shown in Fig. 10. The binding constant (K*a*) values are calculated using the following Benesi-Hildebrand equation (1) and which are tabulated in Table (6).

$$\frac{A_0}{A-A_0} = \frac{\varepsilon_G}{\varepsilon_v} + \left(\frac{\varepsilon_G}{\varepsilon_c . K_\alpha}\right) X \frac{1}{[G]} \qquad (1)$$

Where A_0 and A represent the absorbance of ovalbumin, in the absence and presence of prepared nanoparticles respectively. [G] denotes the concentration of prepared nanoparticles. ε_G is the molar extinction coefficient of the prepared nanoparticles. ε_v &ε_c are their respective molar extinction coefficient of the free Ovalbumin and Ovalbumin bounded nanoparticles respectively. A linear double reciprocal plot of $1/A\text{-}A_0$ vs $1/[G]$ can be used to calculate the binding constant (K*a*).

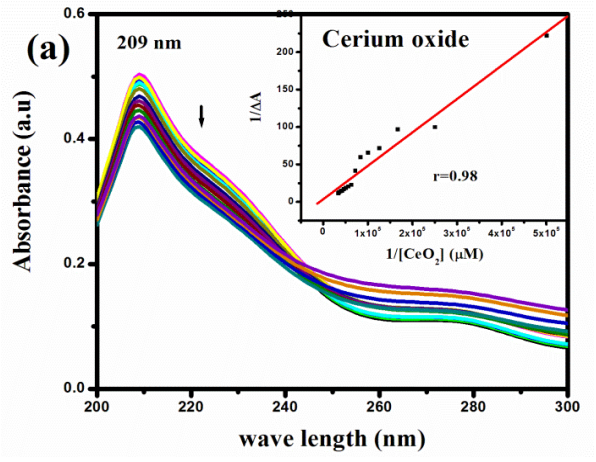

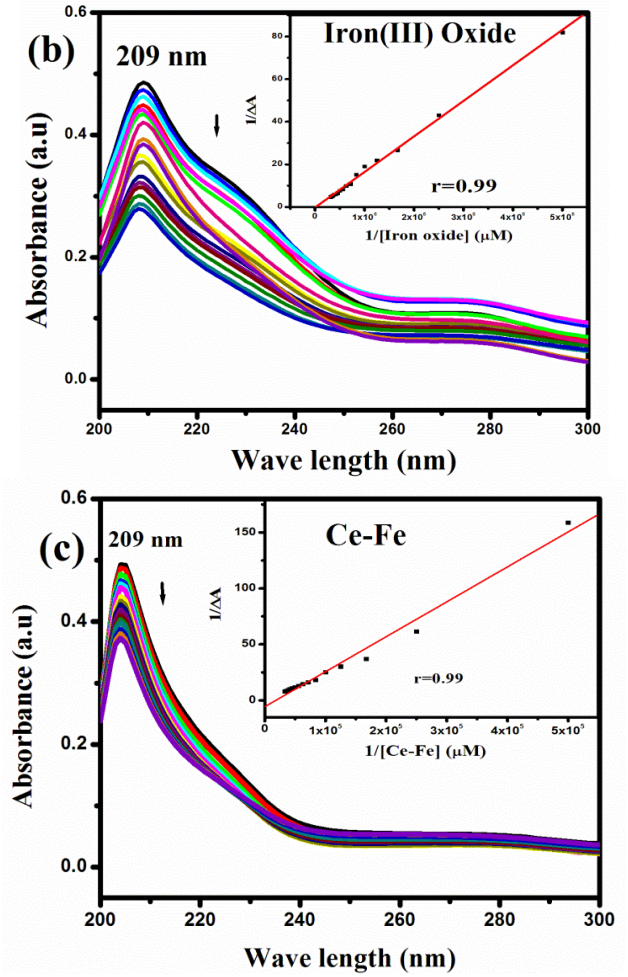

Figure.10. UV-visible absorption spectra of ovalbumin (20 μM) upon gradual addition of various concentrations (0 to 30 μM) of (a) Cerium oxide, (b) Iron(III) oxide and (c) CFMMO (Ce-Fe) Inset **:** linear double reciprocal plot.

Fluorescence spectral responses of Ovalbumin

A comprehension of Ovalbumin's structural and functional properties can be gained by examining its fluorescence spectral responses [60]. A widely used technique in the field of molecular spectroscopy for examining the interactions between fluorescent molecules and quenchers is fluorescence spectral titrations quenching, or fluorescence quenching. This technique evaluates how the presence of a quencher reduces the fluorescence intensity of a fluorescent analyte. Many molecular interactions, including energy transfer, molecular rearrangements, ground state complex formation, excited state reactions, and collisional diffusion, lead to fluorescence quenching. Dynamic quenching or state quenching techniques can be used to cause quenching during these interactions. When an excited state fluorophore collides with a quencher molecule in a solution, the intensity of the fluorescence decreases, a phenomenon known as dynamic quenching. The fluorophore returns to its ground state through diffusion during an interaction with the quencher, forming a ground state complex with the quencher, and causing static quenching.

Fluorescence titration analysis was used to determine the nanoparticle's ability to bind with the ovalbumin. When excited at 280 nm, ovalbumin's fluorescence emission spectrum peak was appeared at 331 nm for Cerium oxide, Iron(III) oxide and CFMMO (Ce-Fe). The emission intensity of Ovalbumin was quenched due to the interaction of nanoparticles with Ovalbumin. Using the Stern-Volmer equation, the quenching parameters were calculated using the following equation (2).

$$\frac{F_0}{F} = 1 + K_{SV} = 1 + k_q \tau_0 \qquad (2)$$

Where F_0 and F denotes the fluorescence intensities of Ovalbumin in the absence and presence of prepared nanoparticles. K_{sv} is the Stern-Volmer constant, and τ_0 represents Ovalbumin lifetime 10^{-8}s (ι) without any quencher. The intensity of the fluorescence decreases as the concentration of prepared nanoparticles increases, from 0 to 30 μM, when added to a fixed concentration of ovalbumin (20 μM). This decrease in intensity is due to the interaction between the nanoparticles and ovalbumin, as shown in Fig.11. The modified Benesi-Hildebrand plot is also shown in the inset [Fig.11(a,b,c)]. The Stern-Volmer plot was created and shown in Fig.12 using the emission spectral data and the values for the Stern-Volmer constant (K_{sv}) and bimolecular quenching constant (k_q) were calculated and recorded in Table 6. The apparent binding constant values (K_{app}) are also calculated from the plot of log[(F_0-F)/F vs log[Q]. The slope value n which gives the number of binding sites for all the prepared compounds are calculated using the following scatchard equation (3) and shown in Table 6.

$$\log\,[F_0 - F)\,/F] = \log\ \mathrm{Kapp} + \mathrm{n}\log\,[\mathrm{Q}] \qquad (3)$$

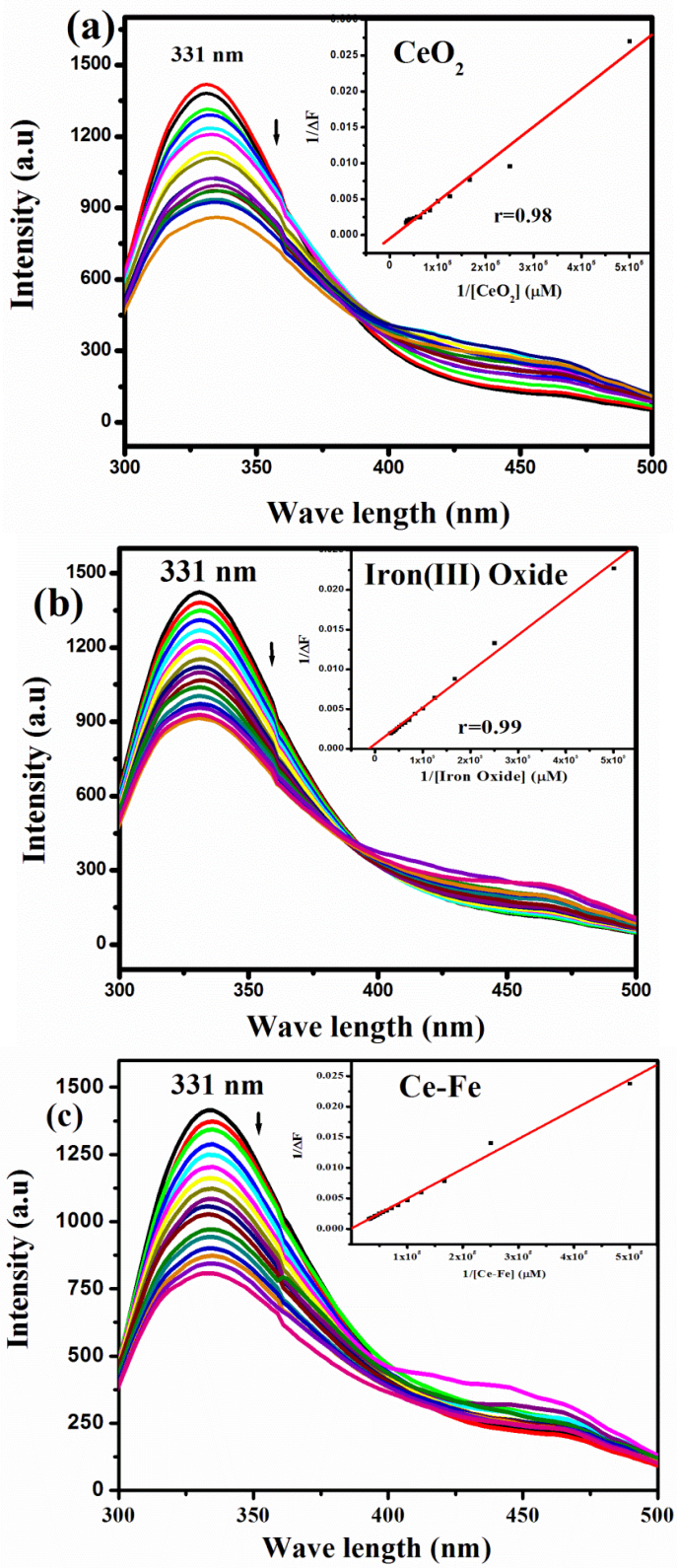

Figure.11. Fluorescence emission spectra of Ovalbumin (20 μM) upon gradual addition of various concentrations (0-30 μM) of (a) Cerium oxide, (b) Iron(III) oxide and (c) CFMMO (Ce-Fe) Inset : Modified Benesi-Hildebrand plot.

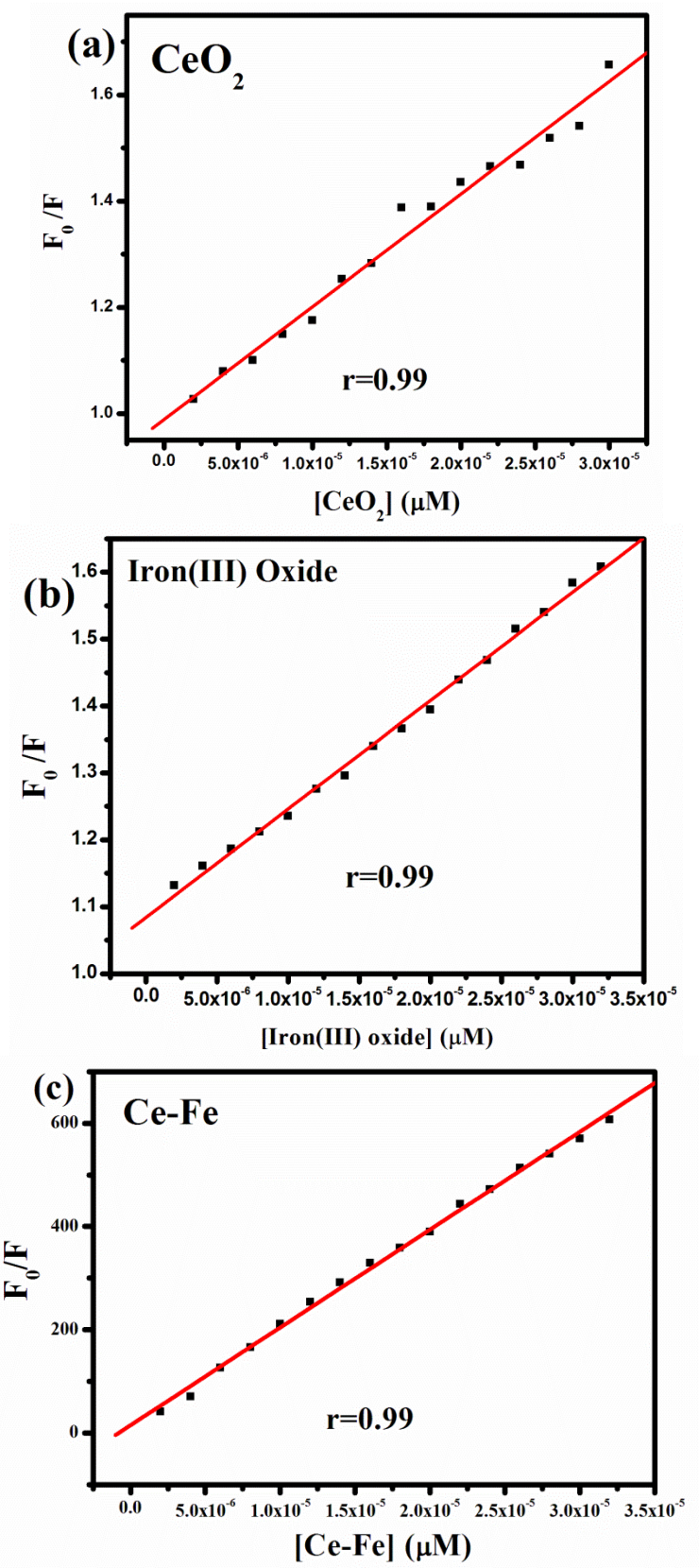

Figure.12. Stern-Volmer plot of (a) Cerium oxide, (b) Iron(III) oxide and (c) CFMMO (Ce-Fe)

The interaction between the nanoparticles Cerium oxide, Iron(III) oxide and CFMMO (Ce-Fe) (as shown in the Figures) has been analyzed to determine the binding parameters. The findings show that ovalbumin's intrinsic fluorescence can be considerably suppressed by the metal oxide nanoparticles made in this investigation. Furthermore, 2.90 x $10^{10}M^{-1}S^{-1}$, the generally acknowledged maximum diffusion constant for biomolecules, is exceeded by the obtained quenching rate constant (k_q) [61]. These results imply that the static quenching mechanism defines the binding process between ovalbumin and metal oxide nanoparticles.

Table.6. Binding parameters of nanomaterials with Ovalbumin from spectral data.

S.No	Name of the samples	Absorption (UV)		Emission (Flouresence)					
		λmax (nm)	K*a* (M^{-1})	λem (nm)	K_{sv} (M^{-1})	k_q($M^{-1}s^{-1}$)	K_b(M^{-1})	K_{app}(M^{-1})	n
1	CeO_2	209	$4.31x10^4$	331	$4.65x10^5$	$4.65x10^{13}$	$5.330x10^4$	$8.62x10^4$	1.13
2	Fe_2O_3	209	$1.30x10^4$	331	$5.39x10^5$	$5.39x10^{13}$	$1.26x10^4$	$3.77x10^4$	1.07
3	Ce-Fe	209	$4.80x10^4$	331	$7.02x10^5$	$7.02x10^{13}$	$1.82x10^5$	$1.43x10^5$	1.18

Antibacterial activity of cerium oxide, Iron(III) oxide and cerium iron mixed metal oxide (CFMMO)

cerium oxide, Iron(III) oxide and CFMMO are remarkable compounds that have garnered significant attention in the world of antibacterial research. These nanoparticles exhibit unique properties that make them highly effective against a wide range of bacteria [62]. These compounds exhibit promising properties, offering a new perspective on antibacterial treatments [63]. This research work used the disc diffusion method to investigate the intriguing antibacterial activity of cerium oxide, Iron(III) oxide and CFMMO against the bacterial strains *E. Coli, Bacillus subtilis, Bacillus cereus, Pseudomonas aeruginosa, and Staphylococcus aureus*. In this method, the test bacteria were introduced into peptone water and left to incubate at a temperature of 35ºC for a period of 3 to 4 hours. Subsequently, sterile petri plates containing Mueller Hinton agar were prepared and poured into them. A volume of 0.1 ml of bacterial culture was then placed on the surface of the agar plates, which were later spread evenly using an L-rod. After allowing the inoculated plates to dry for five minutes, a disk loaded with a concentration of 1000 µg/ml of the tested sample was carefully placed on top of the inoculated petri plates using sterile techniques. The plates were incubated at a temperature of 37ºC for a duration of 18 to 24 hours. Following incubation, the plate is examined for the presence of a zone of inhibition, which is then measured in millimeters. Remarkably, all three nanoparticles exhibit notable antibacterial activities, effectively hindering the growth of pathogens. The highest zone of inhibition, measuring 19 mm, was observed for CFMMO (Ce-Fe) against the bacterium *Pseudomonas aeruginosa*. The antibacterial activities of CFMMO against the various bacterial strains are shown in Fig. 13. The antibacterial activity zone of inhibition images for CeO_2, Fe_2O_3 and CFMMO are shown in Figure 14 and the zone of inhibition values are given in Table 7.

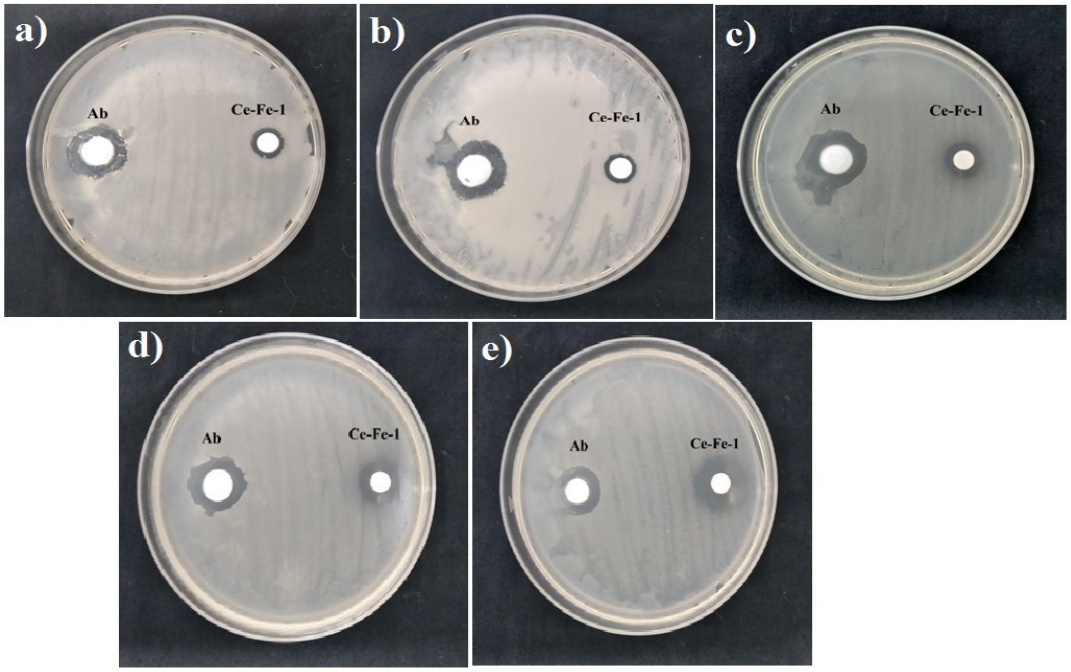

Figure.13. Antibacterial activity of Ce-Fe mixed metal oxide for (a) E. Coli, (b) Bacillus subtilis, (c) Bacillus cereus, (d) Pseudomonas aeruginosa, and (e) Staphylococcus aureus bacterial strains

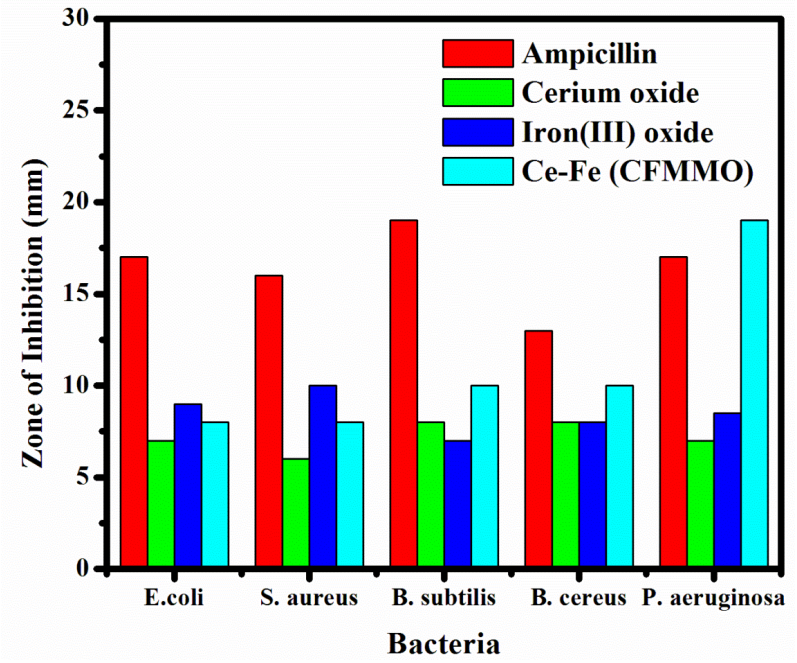

Figure.14. Bar graphs for Antibacterial activity Zone of inhibition levels for CeO_2, Fe_2O_3 and CFMMO

Table.7. Antibacterial activity Zone of inhibition levels for CeO_2, Fe_2O_3 and CFMMO

Bacteria	Inhibition zone in mm			
	Ab Ampicillin	CeO_2	Fe_2O_3	CFMMO
E.coli	17	7	9	8
Staphylococcus aureus	16	6	10	8
Bacillus subtilis	19	8	7	10
Bacillus cereus	13	8	8	10
Pseudomonas aeruginosa	17	7	8.5	19

CONCLUSION

The microwave-assisted co-precipitation process was utilized to synthesize cerium oxide, iron oxide, and mixed metal oxides of CFMMO. The synthesized nanoparticles were characterized using FT-IR, UV-VIS (DRS), XRD, FE-SEM, AFM, and EDAX. FE-SEM was employed to analyze the surface morphology of the metal oxide nanoparticles, revealing various morphological features. The structure of the synthesized product as nanocrystallites was confirmed by XRD data. The XRD pattern also confirmed the face-centered rhombohedral lattice of α-Fe2O3 nanoparticles and the cubic fluorite structure of CeO2. The composition of the samples was determined by EDAX, which verified high levels of cerium oxide (96.86%), iron oxide (100.0%), and CFMMO (100.0%) purity. Ammonia on CFMMO's mixed metal oxides and hydrogen sulfide on cerium oxide and mixed metal oxides exhibit distinct and strong oxidation peaks in the electrochemical investigations of cyclic voltammetry, indicating improved sensing performance. The sensitivity, selectivity, and stability of mixed metal oxide-based gas sensors make them a promising option for the detection of hydrogen sulfide and ammonia, according to this study. The nanoparticles prepared were quenched by Ovalbumin through the static quenching process, as the quenching rate constant (kq) exceeded the generally accepted maximum diffusion constant for biomolecules (2.90 x 10^10 M-1S-1). Emission spectral data was used to create a Stern-Volmer plot, from which the Stern-Volmer constant (Ksv) and bimolecular quenching constant (kq) were determined. Additionally, apparent binding constant values (Kapp) were obtained. The prepared compounds showed strong antimicrobial activity against a variety of bacteria, including E.coli, Bacillus subtilis, Bacillus cereus, Pseudomonas aeruginosa, and Staphylococcus aureus. Specifically, the antibacterial effectiveness was 51.82% for iron oxide, 43.90% for cerium oxide, and 67.07% for Ce-Fe mixed metal oxide. It is worth noting that the Ce-Fe mixed metal oxide had the highest zone of inhibition at 19 mm against Pseudomonas aeruginosa. These results indicate that the compounds could be potential alternatives to traditional antibiotics in combating antibiotic resistance. Moreover, the study highlights the enhanced gas detection capabilities of the mixed metal oxides, suggesting possible advancements in gas sensor materials.

REFERENCES

- Chavali, MS, & Nikolova, M.P 2019, 'Metal oxide nanoparticles and their applications in nanotechnology', SN applied sciences, vol.1, no.6, pp.607.
- Rao, R, Pint, CL, Islam, AE, Weatherup, RS, Hofmann, S, Meshot, ER, & Hart, AJ 2018, 'Carbon nanotubes and related nanomaterials: critical advances and challenges for synthesis toward mainstream commercial applications', ACS nano, vol.12 no.12, pp.11756-11784.
- Uskokovic, V 2009, 'Challenges for the modern science in its descend towards nano scale', Current Nanoscience, vol.5, no.3, pp.372-389.
- Malik, S, Muhammad, K, & Waheed, Y 2023, 'Nanotechnology: A revolution in modern industry', Molecules, vol.28, no.2, pp.661.
- Khan, Y, Sadia, H, Ali Shah, SZ, Khan, MN, Shah, AA, Ullah, N, & Khan, MI 2022, 'Classification, synthetic, and characterization approaches to nanoparticles and their applications in various fields of nanotechnology: A review', Catalysts, vol.12, no.11, pp.1386.
- Jeevanandam, J, Barhoum, A, Chan, Y S, Dufresne, A, & Danquah, MK 2018, 'Review on nanoparticles and nanostructured materials: history, sources, toxicity and

regulations', Beilstein journal of nanotechnology, vol.9, no.1, pp.1050-1074.
- Takai, T, Shibatani, A, Asakuma, Y, Saptoro, A, & Phan, C 2022, 'Microwave-assisted nanoparticle synthesis enhanced with addition of surfactant', Chemical Engineering Research and Design, no.182, pp.714-718.
- Gabano, E, & Ravera, M 2022, 'Microwave-Assisted Synthesis: Can Transition Metal Complexes Take Advantage of This Green Method ?', Molecules, vol.27, no.13, p.4249.
- Saleem, Q, Torabfam, M, Fidan, T, Kurt, H, Yuce, M, Clarke, N, & Bayazit, M.K 2021, 'Microwave-Promoted Continuous Flow Systems in Nanoparticle Synthesis—A Perspective', ACS Sustainable Chemistry & Engineering, vol.9, no.30, pp.9988-10015.
- Aboud, A.A, Al-Kelesh, H, El Rouby, W.M, Farghali, A.A, Hamdedein, A, & Khedr, M.H 2018, 'CO2 responses based on pure and doped CeO2 nano-pellets', Journal of materials research and technology, vol.7, no.1, pp.14-20.
- Chu, T.D, Quach, D.T, Nguyen, X.T, Nguyen, T.S, Pham, D.T. & Kim, D.H 2020, 'Synthesis and properties of magnetic-semiconductor Fe_3O_4/TiO_2 heterostructure nanocomposites for applications in wastewater treatment', Journal of Magnetics, vol.25, no.1, pp.1-7.
- D'Souza, L, & Richards, R 2007, 'Synthesis of metal-oxide nanoparticles: liquid–solid transformations', Synthesis, properties, and applications of oxide nanomaterials. Hoboken, New Jersey: John Wiley & Sons, Inc, pp.81-117.
- Arora, A.K, Jaswal, V.S, Singh, K, & Singh, R 2016, 'Applications of metal/mixed metal oxides as photocatalyst:(A review)', Oriental Journal of Chemistry, vol.32, no.4, pp.2035.
- Stankic, S, Suman, S, Haque, F, & Vidic, J 2016, 'Pure and multi metal oxide nanoparticles: synthesis, antibacterial and cytotoxic properties', Journal of nanobiotechnology, vol.14, no.1, pp.1-20.
- Quispe, L.T, Mamani, L.L, Baldárrago-Alcántara, A.A, Félix, L.L, Goya, G.F, Fuentes-García, J.A, Pacheco-Salazar, D.G, & Coaquira, J.A 2022, 'Synthesis and characterization of α-Fe_2O_3 nanoparticles showing potential applications for sensing quaternary ammonium vapor at room temperature', Nanotechnology, vol.33, no.33, pp.335704.
- Teng, Y, Zhang, X.F, Xu, T.T, Deng, Z.P, Xu, Y.M, Huo, L.H, & Gao, S 2020, 'A spendable gas sensor with higher sensitivity and lowest detection limit towards H_2S: porous α-Fe_2O_3 hierarchical tubule derived from poplar branch', Chemical Engineering Journal, vol.392, pp.123679.
- Besenhard, M.O, LaGrow, A.P, Hodzic, A, Kriechbaum, M, Panariello, L, Bais, G, Loizou, K, Damilos, S, Cruz, M.M, Thanh, N.T.K. & Gavriilidis, A 2020, 'Co-precipitation synthesis of stable iron oxide nanoparticles with NaOH: New insights and continuous production via flow chemistry', Chemical Engineering Journal, vol.399, pp.125740.
- Lassoued, A, Dkhil, B, Gadri, A, & Ammar, S 2017, 'Control of the shape and size of iron oxide (α-Fe_2O_3) nanoparticles synthesized through the chemical precipitation method', Results in physics, vol.7, pp.3007-3015.
- Zahmouli, N, Hjiri, M, El Mir, L, Bonavita, A, Donato, N, Neri, G, & Leonardi, S.G 2018, High performance acetone sensor based on γ-Fe_2O_3/Al–ZnO nanocomposites', Nanotechnology, vol.30, no.5, pp.055502.
- Gusain, D, Awolusi, O.O, & Bux, F 2022, 'Synthesis and characterization of iron oxide/MIL-101 composite via microwave solvothermal treatment', Surface Science, vol.716, pp.121952.
- Younis, A, Chu, D, & Li, S 2016, 'Cerium oxide nanostructures and their applications', Nanomater, vol.3, pp.53-68.
- Manjula, N, Pulikkutty, S, Chen, T.W, Chen, S.M, Fan, C.H, Ali, M.A, & Al-Hemaid, F.M 2022, 'Electrochemical sensor based on cerium niobium oxide nanoparticles modified electrode for sensing of environmental toxicity in water samples', Colloids and Surfaces A: Physicochemical and Engineering Aspects, vol.637, pp.128277.
- Zhang, J.W, & Zhang, X 2020, 'Electrode material fabricated by loading cerium oxide nanoparticles on reduced graphene oxide and its application in electrochemical sensor for tryptophan', Journal of Alloys and Compounds, vol.842, pp.155934.
- Lair, V, Ringuedé, A, Vermaut, P, & Griveau, S 2008, 'Synthesis and characterization of cerium oxide by electrochemical methods', physica status solidi c, vol.5, no.11, pp.3492-3495.
- Kosto, Y, Zanut, A, Franchi, S, Yakovlev, Y, Khalakhan, I, Matolin, V, Prince, K.C, Valenti, G, Paolucci, F, & Tsud, N 2019, 'Electrochemical activity of the polycrystalline cerium oxide films for hydrogen peroxide detection', Applied Surface Science, vol.488, pp.351-359.
- Zhang, X, Zhang, W, Du, J, Sun, Q, Yuan, W, Wang, H, & Wu, J, 2023, 'Investigation on morphologies and supporter of cerium dioxide nanostructure on oxime based electrochemical sensors for organophosphorus detection', Microchemical Journal, vol.191, pp.108891.
- Reddy, B.M, Bharali, P, Saikia, P, Thrimurthulu, G, Yamada, Y, & Kobayashi T 2009, 'Thermal Stability and Dispersion Behavior of Nanostructured Ce x Zr1− x O_2 Mixed Oxides over Anatase-TiO_2: A Combined Study of CO Oxidation and Characterization by XRD, XPS, TPR, HREM, and UV− Vis DRS', Industrial & Engineering Chemistry Research, vol.48, no.1,pp.453-462.
- Singh, S.P, Singh, A.K, & Gupta, J 2022, 'Synthesis of nickel-doped iron oxide nanoparticles by Co-precipitation method and investigation of its structural and opto-electronic properties', Materials Today: Proceedings, vol.66, pp.1890-1896.
- Álvarez-Asencio, R, Corkery, R.W, & Ahniyaz, A 2020, RSC advances, vol.10, no.25, pp.14818-14825.
- Kumar, V, Ahlawat, D.S, Islam, S.A, & Singh, A 2021, 'Ce doping induced modifications in structural, electrical and magnetic behaviour of hematite nanoparticles', Materials Science and Engineering: B pp.272:115327.
- S, Bagheri, I, Khalil, N.M, Julkapli, *Journal of Rare Earths.*, **2021**, *39*(2), pp.129-139.
- Ananthanarayanan, D, Leon, J.J.D, Wong, J, Nicolay, S, Aberle, A.G, & Ho J.W 2020, 'Mid-infrared characterization and modelling of transparent conductive oxides', Solar Energy, vol.209, pp.424-430.
- Ridente, E, Mamaikin, M, Altwaijry, N, Zimin, D, Kling, M.F, Pervak, V, Weidman, M, Krausz, F, & Karpowicz ,N 2022, 'Electro-optic characterization of synthesized infrared-visible light fields', Nature communications, vol.13, no.1, pp.1111.
- Ali, M.M, Mahdi, H.S, Parveen, A, & Azam, A 2018, 'Optical properties of cerium oxide (CeO_2) nanoparticles synthesized by hydroxide mediated method', In AIP Conference Proceedings, vol.1953, no.1, AIP Publishing.
- Calvache-Muñoz, J, Prado, F.A, & Rodríguez-Páez, J.E 2017, 'Cerium oxide nanoparticles: Synthesis, characterization and tentative mechanism of particle formation' Colloids and Surfaces A: Physicochemical and Engineering Aspects, vol.529, pp.146-159.
- Kiani D, (2023) X-Ray Diffraction (XRD). In Springer Handbook of Advanced Catalyst Characterization 519-539
- Ali, A, Chiang, Y.W, & Santos, R.M 2022, 'X-ray diffraction techniques for mineral characterization: A review for engineers of the fundamentals, applications, and research directions', Minerals, vol.12, no.2, pp.205.
- Babitha, K.K, Sreedevi, A, Priyanka, K.P, Sabu, B, & Varghese, T 2015 Indian Journal of pure & applied physics, vol.53, no.9, pp.596-603.
- Lassoued, A, Dkhil, B, Gadri, A, & Ammar, S 2017, 'Control of the shape and size of iron oxide (α-Fe_2O_3)

nanoparticles synthesized through the chemical precipitation method', Results in physics, vol.7, pp.3007-3015.
- Umar, A, Abaker, M, Faisal, M, Hwang, S.W, Baskoutas, S, & Al-Sayari, S.A 2011, 'High-yield synthesis of well-crystalline α-Fe_2O_3 nanoparticles: structural, optical and photocatalytic properties', Journal of Nanoscience and Nanotechnology, vol.11, no.4, pp.3474-3480.
- Shirley, B, & Jarochowska, E 2022, 'Chemical characterisation is rough: the impact of topography and measurement parameters on energy-dispersive X-ray spectroscopy in biominerals', Facies, vol.68, no.2, pp.7
- Jalilpour, M, & Fathalilou, M 2012, 'Effect of aging time and calcination temperature on the cerium oxide nanoparticles synthesis via reverse co-precipitation method', Int. J. Phys. Sci, vol.7, no.6, pp.944-948.
- Farahmandjou, M, Zarinkamar, M, & Firoozabadi, T.P 2016, 'Synthesis of Cerium Oxide (CeO_2) nanoparticles using simple CO-precipitation method', Revista mexicana de física, vol.62, no.5, pp.496-499.
- Agarwal, P.B, Paulchowdhury, P, Mukherjee, A, Lohani, P, & Thakur, N.K 2022, 'Optimization of oxygen plasma based etching of single layered graphene through Raman and FESEM characterization', Materials Today: Proce., vol.48, pp.616-618.
- B, Lewczuk, N, Szyrynska, Animals., **2021**, 11, 3390.
- H, Bi, L.X, Zhang, Y, Xing, P, Zhang, J.J, Chen, J, Yin, L.J, Bie, *Sensors and Actuators B:* Chemical., **2021**, *330*, p.129374.
- Nguyen, T.D, & Do, T.O 2011, 'Size-and shape-controlled synthesis of monodisperse metal oxide and mixed oxide nanocrystals', Nanocrystal, vol.66, pp.55-84.
- Ho, T.M, Abik, F, Mikkonen, K.S 2022, 'An overview of nanoemulsion characterization via atomic force microscopy', Critical Reviews in Food Science and Nutrition, vol.62, no.18, pp.4908-4928.
- Mei, L, & Guan, G 2022, 'Profilometry and atomic force microscopy for surface characterization', Nano TransMed, vol.2, no.1, pp.9130017.
- Alsteens, D, Gaub, H.E, Newton, R, Pfreundschuh, M, Gerber, C, & Müller D.J 2017, 'Atomic force microscopy-based characterization and design of biointerfaces', Nature Reviews Materials vol.2, no.5, pp.1-16.
- Muthusankar, G, Sangili, A, Chen, S.M, Karkuzhali, R, Sethupathi, M, Gopu, G, Karthick, S, Devi, R.K, & Sengottuvelan, N 2018, 'In situ assembly of sulfur-doped carbon quantum dots surrounded iron (III) oxide nanocomposite; a novel electrocatalyst for highly sensitive detection of antipsychotic drug olanzapine', Journal of Molecular Liquids, vol.268, pp.471-480.
- Murugappan, K, Lee, J, & Silvester, D.S 2011, 'Comparative study of screen printed electrodes for ammonia gas sensing in ionic liquids', Electrochemistry Communications, vol.13, no.12, pp.1435-1438.
- Borcherding, J, Baltrusaitis, J, Chen, H, Stebounova, L, Wu, C.M, Rubasinghege, G, Mudunkotuwa, I.A, Caraballo, J.C, Zabner, J, Grassian, V.H, & Comellas, A.P 2014, 'Iron oxide nanoparticles induce Pseudomonas aeruginosa growth, induce biofilm formation, and inhibit antimicrobial peptide function', Environmental Science: Nano, vol.1, no.2, pp.123-132.
- Zuñiga, J, Akashi, L, Pinheiro, T, Rivera, M, Barreto, L, Albertin, K.F, & Champi, A 2022, 'Synthesis of lysozyme-reduced graphene oxide films for biosensor applications', Diamond and Related Materials, vol.126, pp.109093.
- Fang, S, Dong, X, Ji, H, Liu, S, Yan, F, Peng, D, He, L, Wang, M, & Zhang, Z 2016, 'Electrochemical aptasensor for lysozyme based on a gold electrode modified with a nanocomposite consisting of reduced graphene oxide, cuprous oxide, and plasma-polymerized propargylamine', Microchimica Acta, vol.183, pp.633-642.
- Shareghi, B, Farhadian, S, Zamani, N, Salavati-Niasari, M, & Gholamrezaei, S 2016, 'Stability and enzyme activity of lysozyme in the presence of Fe 3 O 4 nanoparticles', Monatshefte für Chemie-Chemical Monthly, vol.147, pp.465-471.
- Siddiquee, M.A, ud din Parray, M, Kamli, M.R, Malik, M.A, Mehdi, S.H, Imtiyaz, K, Rizvi, M.M.A, Rajor, H.K, & Patel, R 2021, 'Biogenic synthesis, in-vitro cytotoxicity, esterase activity and interaction studies of copper oxide nanoparticles with lysozyme', Journal of Materials Research and Technology, vol.13, pp.2066-2077.
- Khumsap, T, Bamrungsap, S, Thu, V.T, & Nguyen, L.T 2021, 'Epitope-imprinted polydopamine electrochemical sensor for ovalbumin detection', Bioelectrochemistry, vol.140, pp.107805.
- Fu, H, Bai, Z, Li, P, Feng, X, Hu, X, Song, X, & Chen, L 2023, 'Molecular imprinted electrochemical sensor for ovalbumin detection based on boronate affinity and signal amplification approach', Food Chemistry, vol409, pp.135292.
- Huang, J, Wu, Y, Cong, J, Luo, J, & Liu, X 2018, 'Selective and sensitive glycoprotein detection via a biomimetic electrochemical sensor based on surface molecular imprinting and boronate-modified reduced graphene oxide', Sensors and Actuators B: Chemical, vol.259, pp.1-9.
- Li, M.X, Wang, X.H, Zhang, L.M, & Wei, X.P 2017, 'A high sensitive epitope imprinted electrochemical sensor for bovine serum albumin based on enzyme amplifying', Analytical Biochemistry, vol.530, pp.68-74.
- Pachaiappan, R, Rajendran, S, Show, P.L, Manavalan, K, & Naushad, M 2021, 'Metal/metal oxide nanocomposites for bactericidal effect: A review', Chemosphere, vol.272, pp.128607.
- Moon, K.S, Bae, J.M, Oh, S, & Choi, E.J 2024, 'Enhanced photocatalytic antibacterial activity of Au-coated Ni–Ti–O nanotubes for biomedical applications', Materials Chemistry and Physics, vol.314, pp.128910.